

Probing the anisotropic expansion from supernovae and GRBs in a model-independent way

J. S. Wang ^{*} and F. Y. Wang [†]

School of Astronomy and Space Science, Nanjing University, Nanjing 210093, China

Key Laboratory of Modern Astronomy and Astrophysics (Nanjing University), Ministry of Education, Nanjing 210093, China

24 July 2018

ABSTRACT

In this paper, we study the anisotropic expansion of the universe using type Ia supernovae Union 2.1 sample and 116 long gamma-ray bursts. The luminosity distance is expanded with model-independent cosmographic parameters as a function of $z/(1+z)$ directly. Thus the results are independent of cosmology model. We find a dipolar anisotropy in the direction ($l = 309.2^\circ \pm 15.8^\circ$, $b = -8.6^\circ \pm 10.5^\circ$) in galactic coordinates with a significant evidence 97.29% (more than 2σ). The magnitude is $(1.37 \pm 0.57) \times 10^{-3}$ for the dipole, and $(2.6 \pm 2.1) \times 10^{-4}$ for the monopole, respectively. This dipolar anisotropy is more significant at low redshift from the redshift tomography analysis. We also test whether this preferred direction is caused by bulk flow motion or dark energy dipolar scalar perturbation. We find that the direction and the amplitude of the bulk flow in our results are approximately consistent with the bulk flow surveys. Therefore, bulk flow motion may be the main reason for the anisotropic expansion at low redshift, but the effect of dipolar distribution dark energy can not be excluded, especially at high redshift.

Key words: cosmology: theory, dark energy, Type Ia supernovae

1 INTRODUCTION

The Universe is homogeneous and isotropic on cosmic scales on the basis of the cosmological principle. It is the foundation in modern cosmology. This principle is well con-

^{*} jiesh.wang@gmail.com(JSW)

[†] fayinwang@nju.edu.cn(FYW)

firmed by the precise measurements of cosmic microwave background (CMB) from Wilkinson Microwave Anisotropy Probe (WMAP) (Hinshaw et al. 2013) and *Planck satellite* (Planck Collaboration et al. 2013). However, in the processing of CMB data, the motion of our Local Group of galaxies should be deducted. Kogut et al. (1993) obtained that the peculiar velocity is $627 \pm 22 \text{ km s}^{-1}$ towards ($l = 276^\circ \pm 3^\circ, b = 30^\circ \pm 3^\circ$) using the COBE Differential Microwave Radiometers first year data. Bulk flow velocity on the scales around $50h^{-1} \text{ Mpc}$ is found to be $407 \pm 81 \text{ km s}^{-1}$ towards ($287^\circ \pm 9^\circ, 8^\circ \pm 6^\circ$), roughly close to CMB dipole (Watkins, Feldman & Hudson 2009). But, it's much larger than the expected *rms* bulk flow velocity on the same scale, which is approximately 110 km s^{-1} in the standard ΛCDM normalized with WMAP5 ($(\Omega_m, \sigma_8) = (0.258, 0.796)$). This hints that the universe may have a preferred expanding direction.

Additional evidences for such dipolar anisotropy have been obtained by low multipoles alignment in CMB angular power spectrum (Lineweaver et al. 1996; Tegmark et al. 2003; Bielewicz, Górski & Banday 2004; Frommert & Enßlin 2010), large scale alignments of quasar polarization vectors (Hutsemékers et al. 2005, 2011), dark energy dipole in type Ia supernovae (SNe Ia) (Antoniou & Perivolaropoulos 2010; Mariano & Perivolaropoulos 2012; Yang, Wang & Chu 2014), and the spatial variation in fine-structure constant α (Webb et al. 2011; King et al. 2012). The significances of these dipoles anisotropy are around 2σ . Indeed, many studies using SNe Ia data to test if the universe accelerates isotropically have been done (Kolatt & Lahav 2001; Bonvin, Durrer & Kunz 2006; Gordon, Land & Slosar 2007; Schwarz & Weinhorst 2007; Gupta, Saini & Laskar 2008; Koivisto & Mota 2008a,b; Blomqvist, Mörtzell & Nobili 2008; Cooray, Holz & Caldwell 2010; Gupta & Saini 2010; Cooke & Lynden-Bell 2010; Antoniou & Perivolaropoulos 2010; Campanelli et al. 2011; Koivisto et al. 2011; Colin et al. 2011; Mariano & Perivolaropoulos 2012; Turnbull et al. 2012; Cai & Tuo 2012; Li et al. 2013; Yang, Wang & Chu 2014). These studies of the anisotropic effects are mainly considered to be caused by bulk flow motion or dark energy dipolar distribution on the basis of ΛCDM .

Cai et al. (2013) examined the dark energy anisotropy deviations using the SNe Ia of Union 2 sample and 67 gamma-ray bursts (GRBs) from Liang et al. (2008) and Wei (2010). However, their results show that the anisotropic evidence in ΛCDM doesn't improve much compared to the results from SNe Ia data alone obtained by Mariano & Perivolaropoulos (2012). Thereby, the significance of anisotropy needs to be studied again with the joint of more high-redshift GRBs. On the other hand, dipolar anisotropy can be caused by many mechanisms, for instance, the cosmic bulk flow motion (Colin et al. 2011; Turnbull et al.

2012; Feindt et al. 2013; Li et al. 2013; Rathaus, Kovetz & Itzhaki 2013) and dark energy anisotropy (Koivisto & Mota 2008b; Antoniou & Perivolaropoulos 2010; Perivolaropoulos 2014). Therefore, it's also important to distinguish which mechanism is dominant in the deviation of isotropy.

Cosmological models are assumed in the previous studies, thus, their results of anisotropic expansion are model-dependent. In this paper, we use a model-independent method to study the anisotropic expansion from standard candles, i.e., expanding the luminosity distance using fourth order Hubble series parameters as a function of $z/(1+z)$ directly (Cattoen & Visser 2007; Wang & Dai 2011). This expansion is only dependent on the cosmological principle and the Friedmann-Robertson-Walker (FRW) metric. The Union 2.1 SNe Ia sample (Suzuki et al. 2012) and 116 GRBs (Wang, Qi & Dai 2011) are used in our study.

The structure of this paper is organized as follows: in the next section, we give brief introductions of observational data. We then introduce the method for quantifying the anisotropic expansion effects on luminosity distances and give the significance through Monte Carlo simulation. In section 3, we divide the data set into several portions with two approaches: redshift bins and variable redshift limits, then we analyze the anisotropic expansion in different redshift ranges. In section 4, we test the bulk flow dipole and simplified dark energy dipolar perturbation model as possible mechanisms for anisotropy. Conclusions and discussions are given in section 5.

2 DIPOLAR ANISOTROPIC EXPANSION WITH COSMOGRAPHY PARAMETERS

2.1 Observational data

In analysis, we use the latest Union 2.1 sample (Suzuki et al. 2012) to constrain the dipolar anisotropy, which contains 580 SNe Ia and covers the redshift range $0.015 \leq z \leq 1.414$. To avoid the lack of high redshift data, we also combine the 116 GRB samples, which are compiled and calibrated by Wang, Qi & Dai (2011) and Wang & Dai (2011) (see detailed information including equatorial coordinates in Table 5). The redshift of GRBs reaches up to $z = 8.2$. The equatorial coordinates of these GRBs are taken from NASA/IPAC Extragalactic Database ¹.

¹ <http://ned.ipac.caltech.edu/forms/byname.html>

We expand the luminosity distance d_L in terms of Hubble series parameters: Hubble parameter (H), deceleration (q), jerk (j) and snap (s) parameter. These four parameters are the first, second, third and fourth derivatives of the scale factor a in the Taylor expansion, respectively. They are model-independent and obtained only from the FRW metric. The definitions of the cosmography parameters can be expressed as follows,

$$\begin{aligned} H &= \frac{\dot{a}}{a}, & q &= -\frac{1}{H^2} \frac{\ddot{a}}{a}, \\ j &= \frac{1}{H^3} \frac{\dot{\ddot{a}}}{a}, & s &= \frac{1}{H^4} \frac{\ddot{\ddot{a}}}{a}. \end{aligned} \quad (1)$$

Visser (2004) expands the luminosity distance as a function of z with the cosmography parameters, which have been studied using observational data (Wang, Dai & Qi 2009a,b). However, it diverges at high redshift, and the GRB data reaches up to a high redshift $z = 8.2$. To avoid this problem, Cattoen & Visser (2007) recast the d_L with improved parameter $y = z/(1+z)$. Therefore, the redshift range $z \in (0, \infty)$ can be mapped into $y \in (0, 1)$. The luminosity distance can be expanded as a function of y as following on the assumption of flat Universe (Cattoen & Visser 2007),

$$\begin{aligned} d_L(y) &= \frac{c}{H_0} \left\{ y - \frac{1}{2}(q_0 - 3)y^2 + \frac{1}{6} [11 - 5q_0 - j_0] y^3 \right. \\ &\quad \left. + \frac{1}{24} [50 - 7j_0 - 26q_0 + 10q_0j_0 + 21q_0^2 - 15q_0^3 + s_0] y^4 + O(y^5) \right\}, \end{aligned} \quad (2)$$

where H_0 , q_0 , j_0 , s_0 are the current values. Then the distance modulus can be derived,

$$\mu_{th} = 5 \log \frac{d_L}{\text{Mpc}} + 25. \quad (3)$$

The best-fit cosmography parameters can be obtained by minimizing the χ^2 , which is constructed as follow,

$$\chi^2(H_0, q_0, j_0, s_0) = \sum_{i=1}^{580} \frac{[\mu_{SNe}(z_i) - \mu_{th}(z_i)]^2}{\sigma_{\mu,i}^2} + \sum_{i=1}^{116} \frac{[\mu_{GRB}(z_i) - \mu_{th}(z_i)]^2}{\sigma_{\mu,i}^2}, \quad (4)$$

where μ_{SNe} and $\sigma_{\mu,i}$ are the observed distance modulus and error bars, μ_{GRB} and $\sigma_{\mu,i}$ are taken from Wang & Dai (2011).

2.2 Anisotropic deviation effects on luminosity distance

We convert the equatorial coordinates of each SNe Ia and GRB sample to galactic coordinates (see in Figure 1), then we find their unit vectors \hat{n}_i in Cartesian coordinates

$$\hat{n}_i = \cos(b_i) \cos(l_i) \hat{i} + \cos(b_i) \sin(l_i) \hat{j} + \sin(b_i) \hat{k}. \quad (5)$$

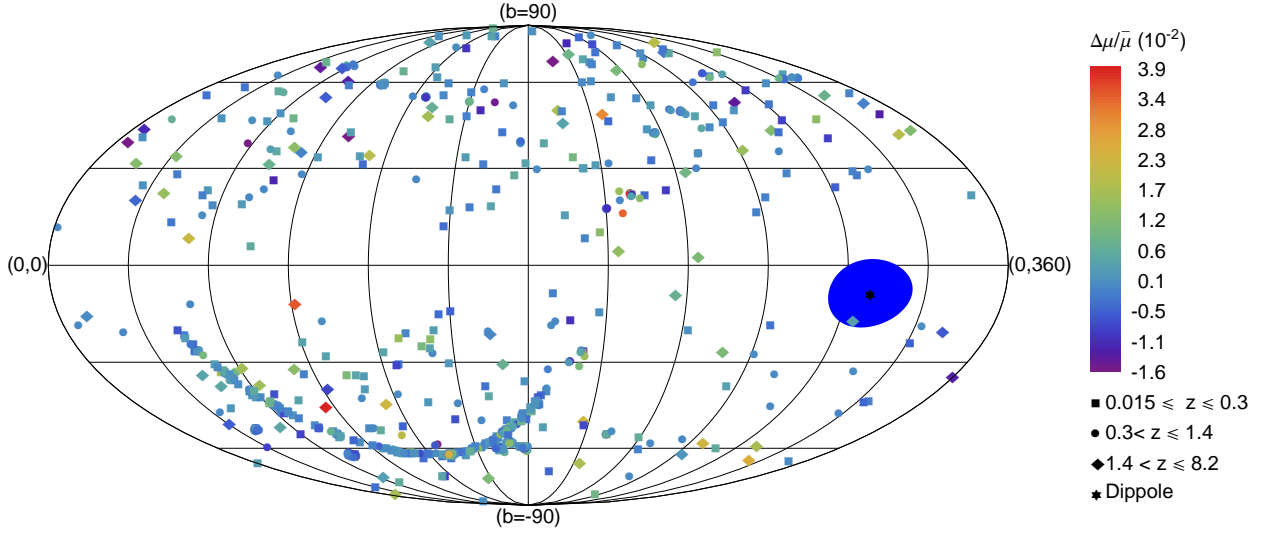


Figure 1. SNe Ia, GRB samples, and the dipolar expansion direction in the galactic coordinates. The data points are divided into three redshift bins with different shapes, the color relates to the redshift. The dark blue blob is the 1σ error of the anisotropic expansion dipole.

In order to quantify the anisotropic deviations on luminosity distance, we define the deviations of distance modulus from the best fit isotropic configuration as follows,

$$\frac{\Delta\mu(z)}{\bar{\mu}(z)} \equiv \frac{\bar{\mu}(z) - \mu_{\text{obs}}(z)}{\bar{\mu}(z)}, \quad (6)$$

where $\bar{\mu}$ are the distance modulus in the context of best-fit cosmography parameters, which are calculated in section 2.1, that is $\bar{\mu} = \mu_{th}$.

We use a dipole model in the direction, $\vec{D} \equiv c_1\hat{i} + c_2\hat{j} + c_3\hat{k}$ and a monopole B ,

$$\left(\frac{\Delta\mu(z)}{\bar{\mu}(z)}\right)_i = \hat{n}_i \cdot \vec{D} - B = A \cos \theta - B, \quad (7)$$

where $A = \sqrt{c_1^2 + c_2^2 + c_3^2}$ and B are the magnitudes of the dipole and monopole, respectively.

To fit the models with the SNe Ia and GRB data, we construct the χ^2 ,

$$\chi^2(\vec{D}, B) = \sum_{i=1}^{696} \frac{\left[\left(\frac{\Delta\mu(z)}{\bar{\mu}(z)}\right)_i - A \cos \theta_i + B\right]^2}{\sigma_i^2}, \quad (8)$$

where $\sigma_i \equiv \frac{\sigma_{\mu,i}}{\bar{\mu}_i(z)}$ are the 1σ errors in data sets.

We find the dipole points to the direction ($b = -8.6^\circ \pm 10.5^\circ$, $l = 309.2^\circ \pm 15.8^\circ$), which is shown in Figure 1. The black star is the dipolar expansion direction, and the dark blue blob is the 1σ error region. The magnitudes of the dipole and monopole are $A = (1.37 \pm 0.57) \times 10^{-3}$ and $B = (2.6 \pm 2.1) \times 10^{-4}$, respectively. It's approximately consistent with the results from Mariano & Perivolaropoulos (2012), Cai et al. (2013), and Yang, Wang & Chu (2014), which are based on Λ CDM model.

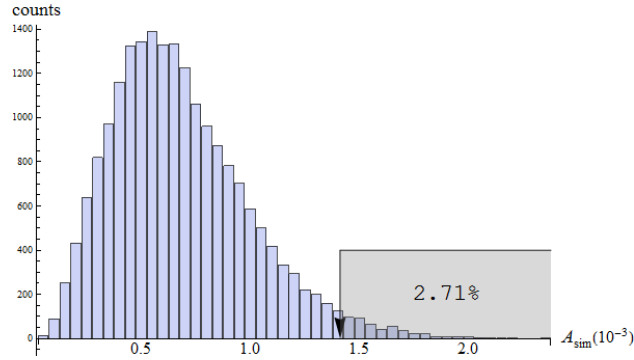


Figure 2. 2×10^5 MC simulations in total have been divided into 47 bins. x-axis is the simulated dipole magnitude bin (A_{sim}) in units of 10^{-3} , y-axis is the counts of each bin. The magnitude of dipole from observed data $A_{\text{obs}} = 1.37 \times 10^{-3}$ lies at the arrow points.

2.3 Significance of dipolar anisotropy

Our results show that the monopole is not significant, while implies the dipolar anisotropy, around 2σ in the relative errors. To obtain the confidence level of dipole anisotropy precisely, we use the Monte Carlo (MC) simulations.

We define new distance modulus (μ') through a Gaussian random selection function, i.e. new distance modulus (μ') will be obtained by the normal distribution with mean values $\bar{\mu}$ and standard deviations σ_{μ}^2 from the observed data. We then take place of the observed distance modulus μ_{obs} with the newly constructed μ' , while use the same observed redshift, standard deviations and coordinates in the observed data.

The analysis method is similar to the method in section 2.2. Then, we obtain a new magnitude (A_{sim}) of the dipolar anisotropy in each simulation. We do 2×10^5 MC simulations in total, and divide them into 47 bins. Figure 2 illustrates the probability of each bin value (A_{sim}). The x-axis is the simulated dipole magnitude (A_{sim}) in units of 10^{-3} , and the y-axis is the count of each bin. The arrow points to the dipole magnitude (A_{obs}) obtained with observed data. The results show that the probability that we can observe the magnitude A_{obs} at 1.37×10^{-3} is 2.71%, i.e. the confidence level of the dipolar anisotropy is 97.29%, larger than 2σ (95.4%). It's more significant than the results from SNe Ia Union 2 data (Mariano & Perivolaropoulos 2012) and Union 2.1 data (Yang, Wang & Chu 2014) alone, which give the probability 95.25% and 95.45%, respectively. Therefore, our result shows the significance of dipolar expansion amplitude grows larger with the combination of GRB sample. We also show the evolution of the confidence level with the increasing MC simulations in Figure 3. It illustrates that 2×10^5 MC simulations are enough to converge.

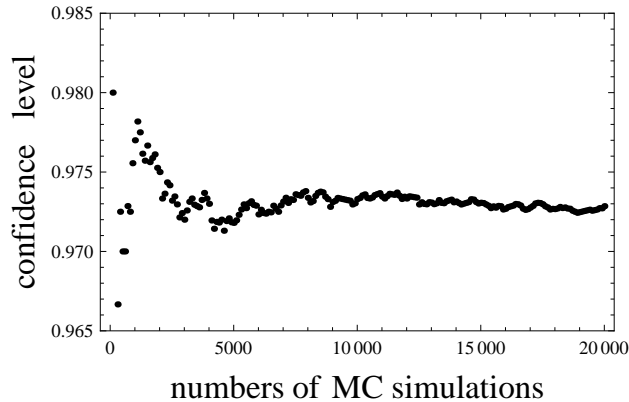


Figure 3. The confidence level of the observed magnitude A_{obs} vs number of MC. x-axis is the MC simulations number of times, y-axis is the confidence level that we can observe the dipole magnitude at $A_{\text{obs}} = 1.37 \times 10^{-3}$.

3 REDSHIFT TOMOGRAPHY

In this section, we focus on the anisotropic effects in different redshift ranges. We use two approaches to study these effects and compare the results with respect to error bar sizes, which relate to the confidence level. The first approach is changing the redshift upper or lower limits, and the second one is dividing the data into 6 redshift bins. The same analysis procedure presented in section 2 are used in each redshift range. The number of data points are approximately equal in each redshift bin, and we define an average redshift of each bin. The variable upper limits method starts from the upper limit $z = 0.035$, approximately $100h^{-1}$ Mpc. Then we increase the upper limit within six steps. The variable lower limit method starts from $z = 0.1$, then we increase it in three steps.

Our results in different redshift ranges are shown in Table 1. The results show that the Union 2.1 data constraints are more stringent than GRB data. This is obvious because of the smaller error bars of SNe Ia luminosity distances comparing with GRBs. The results from variable redshift upper limits method show that the monopole, dipole magnitudes, and the direction converge with the increasing data points. Most of the results are consistent with the full data, except the lowest redshift range. For the variable lower limits way, the magnitudes of dipole is $(0.5 \pm 0.8) \times 10^{-3}$ and $(0.7 \pm 0.8) \times 10^{-3}$ in redshift ranges $0.1 \leq z \leq 8.2$ and $0.4 \leq z \leq 8.2$, respectively. Therefore, these results don't show significant anisotropy at these high redshift ranges, because of their large relative errors.

The redshift bins methods show the anisotropy direction changes randomly with redshift. The magnitudes of monopole and dipole don't show significant evolution with the redshift (see Figures 4 and 5), except for the redshift range $1.4 \leq z \leq 8.2$, but this bin only contains 67 sample, while covers a large redshift range. We find that the lowest redshift

| Redshift range | $B(10^{-4})$ | $A(10^{-3})$ | $b(^{\circ})$ | $l(^{\circ})$ | Data points | Average redshift |
|---------------------------|-----------------|----------------|------------------|------------------|-------------|------------------|
| $0.015 \leq z \leq 8.2$ | 2.5 ± 2.1 | 1.4 ± 0.6 | -8.6 ± 10.5 | 309.2 ± 15.8 | 696 | |
| Union2.1 data | 2.7 ± 2.2 | 1.4 ± 0.6 | -9.0 ± 10.0 | 309.5 ± 15.1 | 580 | |
| GRB data | 34.1 ± 19.4 | 4.2 ± 3.0 | 60.7 ± 51.2 | 313.2 ± 93.8 | 116 | |
| $0.015 \leq z \leq 0.035$ | 2.0 ± 5.7 | 2.8 ± 1.0 | 6.5 ± 17.9 | 300.0 ± 19.5 | 114 | |
| $0.015 \leq z \leq 0.3$ | 3.7 ± 2.7 | 1.8 ± 0.7 | -5.4 ± 12.1 | 304.8 ± 15.2 | 296 | |
| $0.015 \leq z \leq 0.5$ | 2.7 ± 2.5 | 1.3 ± 0.7 | -6.9 ± 13.8 | 296.9 ± 19.0 | 416 | |
| $0.015 \leq z \leq 1.0$ | 2.5 ± 2.2 | 1.4 ± 0.6 | -9.3 ± 10.6 | 308.4 ± 15.7 | 584 | |
| $0.015 \leq z \leq 3.0$ | 2.6 ± 2.1 | 1.4 ± 0.6 | -8.1 ± 10.4 | 309.0 ± 15.7 | 671 | |
| $0.1 \leq z \leq 8.2$ | 1.3 ± 2.9 | 0.5 ± 0.8 | -0.8 ± 36.2 | 289.1 ± 53.6 | 522 | |
| $0.4 \leq z \leq 8.2$ | 0.8 ± 3.8 | 0.7 ± 0.8 | -0.3 ± 35.5 | 18.9 ± 80.6 | 341 | |
| $0.015 \leq z \leq 0.1$ | 4.2 ± 3.6 | 2.1 ± 0.7 | -10.8 ± 12.9 | 319.8 ± 19.1 | 174 | 0.036 |
| $0.1 < z \leq 0.3$ | 6.5 ± 6.2 | 1.4 ± 2.0 | 9.7 ± 55.3 | 284.5 ± 39.7 | 122 | 0.21 |
| $0.3 < z \leq 0.5$ | 16.6 ± 6.6 | 3.8 ± 2.0 | -3.4 ± 9.7 | 331.2 ± 15.4 | 120 | 0.40 |
| $0.5 < z \leq 0.8$ | 3.8 ± 5.2 | 2.3 ± 1.3 | -27.7 ± 16.1 | 348.3 ± 40.7 | 110 | 0.63 |
| $0.8 < z \leq 1.4$ | 13.0 ± 8.0 | 2.1 ± 1.8 | 12.1 ± 27.1 | 340.8 ± 55.5 | 103 | 1.02 |
| $1.4 < z \leq 8.2$ | 73.9 ± 27.0 | 10.1 ± 4.2 | 56.2 ± 28.2 | 345.7 ± 43.4 | 67 | 2.9 |

Table 1. Monopole (B), dipole (A) magnitudes and directions (l, b) in the different redshift ranges of SNe Ia Union 2.1 and GRB data. The number of data points in each range is also given. The average redshift is the average of all the data's redshift in each redshift bin.

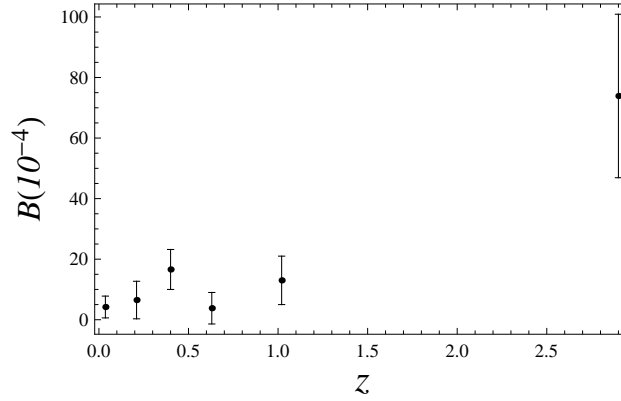


Figure 4. Magnitude of monopole (B) vs the average redshift in GRB and Union 2.1 data.

bin ($0.015 < z \leq 0.1$) show the most significant evidence for dipolar anisotropy with the smallest 1σ relative errors, namely, $(2.1 \pm 0.7) \times 10^{-3}$. While other bins show weaker evidences for anisotropy. Because of their random directions, the total effects are even much weaker, which can be obtained from their magnitude: $(0.5 \pm 0.8) \times 10^{-3}$ in the range of $0.1 \leq z \leq 8.2$ and $(0.7 \pm 0.8) \times 10^{-3}$ in $0.4 \leq z \leq 8.2$. Thus, the significant dipolar anisotropy of the full data is mainly caused by the low redshift sample.

4 POSSIBLE MECHANISM FOR DIPOLAR ANISOTROPY

We have studied the anisotropic expansion with SNe Ia and GRB luminosity distances. We find that the probability of such a dipolar anisotropy is more than 2σ , and it mainly originates from the low redshift data. While the monopole is not significant. Thus, in this section, we try to study two possible mechanisms for dipolar anisotropy. We use bulk flow motion model and

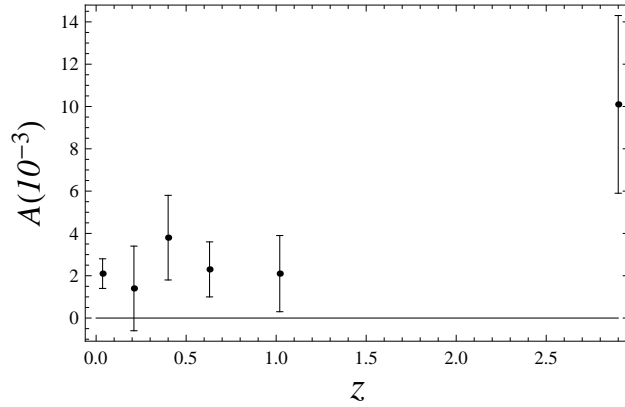


Figure 5. Magnitude of dipole (A) vs the average redshift in GRB and Union 2.1 data.

simplified scalar perturbation metric model caused by dark energy dipolar distributions to fit the same data. However, our methods to quantify the magnitudes of bulk flow motion and dark energy perturbation are simplified. For the careful study of these effects, we need to use the velocity field (Koivisto & Mota 2008a; Li et al. 2013) and anisotropy dark energy model (Koivisto & Mota 2006, 2008b; Mariano & Perivolaropoulos 2012). Since the magnitudes of anisotropy are very small, our results are still reliable.

4.1 Bulk flow motion

Bulk flow motion can affect the Hubble Parameter $H = \frac{v}{D}$ directly, where D is the co-moving distance. Many methods have been taken to analyze this effect on SNe Ia data (Bonvin, Durrer & Kunz 2006; Colin et al. 2011; Feindt et al. 2013; Rathaus, Kovetz & Itzhaki 2013). We choose one method of them to reconstruct the luminosity distance (Bonvin, Durrer & Kunz 2006) as follows

$$d'_L(z) = d_L(z) + \frac{v_{BF} \cdot \hat{n}_i (1+z)^2}{H(z)}, \quad (9)$$

where v_{BF} is the velocity of the bulk flow, $d_L(z)$ is the luminosity distance defined in Eq.(2), and n_i is defined in Eq.(5). The χ^2 is

$$\chi^2(\vec{v}_{BF}) = \sum_{i=1}^{696} \frac{[\mu(d'_L) - \mu_i]^2}{\sigma_i^2}. \quad (10)$$

The results are shown in Table 2. For bulk flow motion, the effects at low redshift ranges are much more attractive. The velocity and direction are $265 \pm 95 \text{ km s}^{-1}$ and $(291.1^\circ \pm 20.6^\circ, -2.7^\circ \pm 15.5^\circ)$ for the full data. On the scale of $100h^{-1} \text{ Mpc}$, i.e. $0.015 \leq z \leq 0.035$, the velocity is $271 \pm 101 \text{ km s}^{-1}$, and the direction points to $(270.0^\circ \pm 20.9^\circ, 10.2^\circ \pm 18^\circ)$. They are approximately consistent with other peculiar velocity surveys shown in Table 3

| Redshift range | v_{BF} (km s ⁻¹) | $b(^{\circ})$ | $l(^{\circ})$ | Data points |
|---------------------------|--------------------------------|-----------------|------------------|-------------|
| $0.015 \leq z \leq 8.2$ | 265 ± 95 | -2.7 ± 15.5 | 291.1 ± 20.6 | 696 |
| Union2.1 data | 254 ± 93 | 0.8 ± 16.5 | 289.7 ± 21.1 | 580 |
| $0.015 \leq z \leq 0.035$ | 271 ± 101 | 10.2 ± 18.0 | 277.0 ± 20.9 | 114 |
| $0.015 \leq z \leq 0.06$ | 252 ± 93 | 8.2 ± 18.6 | 287.2 ± 22.7 | 150 |
| $0.015 \leq z \leq 0.1$ | 240 ± 94 | 7.7 ± 19.6 | 292.2 ± 24.5 | 174 |
| $0.015 \leq z \leq 0.3$ | 248 ± 91 | 3.3 ± 17.1 | 289.2 ± 21.5 | 296 |

Table 2. Bulk flow magnitudes (v_{BF}) and directions (l, b) obtained from the different redshift ranges of SNe Ia Union 2.1 and GRB data, the number of data points in each range are also shown.

| scale | v_{BF} (km s ⁻¹) | $l(^{\circ})$ | $b(^{\circ})$ | Reference |
|------------------------------|--------------------------------|---------------|---------------|---|
| 60 h ⁻¹ Mpc | 225 | 300 | 6 | Hudson et al. (2004) |
| 70 h ⁻¹ Mpc | 330 | 234 | 12 | Sarkar, Feldman & Watkins (2007) |
| 50 ~ 150 h ⁻¹ Mpc | 407 | 287 | 8 | Watkins, Feldman & Hudson (2009); Ma, Gordon & Feldman (2011) |
| 100 h ⁻¹ Mpc | 416 | 282 | 6 | Feldman, Watkins & Hudson (2010) |
| 82.5 h ⁻¹ Mpc | 344.5 | 275.75 | 8 | average |

Table 3. Bulk flow velocities and directions from several surveys. The last row is the average value of each columns.

(Hudson et al. 2004; Sarkar, Feldman & Watkins 2007; Watkins, Feldman & Hudson 2009; Feldman, Watkins & Hudson 2010; Ma, Gordon & Feldman 2011). Their average velocity and direction are 344.5 km s^{-1} and $(275.75^{\circ}, 8^{\circ})$ on the scale $82.5 h^{-1} \text{ Mpc}$. But all the velocities are larger than the expected velocity in ΛCDM .

The direction and velocity of redshift range $0.015 \leq z \leq 0.1$ are consistent with the results from $0.015 \leq z \leq 0.035$. Thus, for this low redshift range, the anisotropy is mainly caused by the bulk flow velocity. The origin for this motion is thought to be the attraction of Shapley Super Cluster (Colin et al. 2011). But this effect could be much weaker at high redshift, because of the larger Hubble flow. Therefore, we can not excluded the dipolar dark energy effects, especially at high redshift.

4.2 Simplified dark energy dipolar scalar perturbation

Another possible anisotropic mechanism is the dark energy dipolar distribution, resulting in dipolar scalar perturbation. For simplification, we use an affected metric imitating the Schwarzschild metric instead of FRW metric,

$$ds^2 = (1 - 2\phi(\vec{x}))dt^2 - a^2(t)(1 + 2\phi(\vec{x}))\delta_{ij}dx^i dx^j. \quad (11)$$

We assume the scalar perturbation field $\phi(\vec{x}) = d \cos \theta$, where θ is the angular between the dipole direction and the observed sample and d is the magnitude of the perturbation.

To determine the perturbed energy-momentum tensor, we base on ΛCDM . Then the luminosity distance can be obtained by solve the Einstein equation (Li et al. 2013),

$$d'_L(z) = \frac{c(1+z)}{H_0} \int_0^z \frac{(1 - d \cos \theta)dx}{\sqrt{\Omega_{m0}(1+x)^3 + 1 - \Omega_{m0} - \frac{4d \cos \theta(1+x)^5}{3H_0^2 d_L^2(z)}}}, \quad (12)$$

| Redshift range | d | $b(^{\circ})$ | $l(^{\circ})$ | Data points |
|---------------------------|--------------------------------|-----------------|-------------------|-------------|
| $0.015 \leq z \leq 8.2$ | $(2.5 \pm 1.0) \times 10^{-5}$ | 6.6 ± 19.9 | 278.2 ± 22.5 | 696 |
| Union2.1 data | $(2.5 \pm 1.0) \times 10^{-5}$ | 6.6 ± 20.0 | 278.2 ± 22.6 | 580 |
| GRB data | $(3.5 \pm 9.0) \times 10^{-2}$ | 17.1 ± 55.0 | 336.3 ± 113.8 | 116 |
| $0.015 \leq z \leq 0.035$ | $(2.6 \pm 1.0) \times 10^{-5}$ | 7.5 ± 20.0 | 274.7 ± 21.9 | 114 |
| $0.015 \leq z \leq 0.1$ | $(2.4 \pm 1.0) \times 10^{-5}$ | 8.6 ± 20.8 | 277.7 ± 23.3 | 174 |
| $0.015 \leq z \leq 0.3$ | $(2.5 \pm 1.0) \times 10^{-5}$ | 6.6 ± 20.0 | 278.2 ± 22.6 | 296 |
| $0.1 \leq z \leq 0.82$ | $(6.3 \pm 8.5) \times 10^{-4}$ | 15.6 ± 48.2 | 241.2 ± 115.6 | 522 |

Table 4. Scalar perturbation magnitude d and direction (l, b) obtained from the different redshift ranges of SNe Ia Union 2.1 and GRB data. The number of data points in each range is also given.

where $d_L(z)$ is defined in Eq.(2) and Ω_{m0} is the current matter density. We use the Eq.(10), and analyze the data in the same way. The results show that the anisotropy amplitude is very small (shown in Table 4). The magnitude of scalar perturbation is $(2.5 \pm 1.0) \times 10^{-5}$, the direction is $(278.2^{\circ} \pm 22.5^{\circ}, 6.6^{\circ} \pm 19.9^{\circ})$. The dipolar evidence in the redshift range $0.1 \leq z \leq 8.2$ is insignificant with large error bar size $(6.3 \pm 8.5) \times 10^{-4}$. But we cannot draw an exact conclusion that the dark energy distributes isotropically or not, because the high redshift sample is sparse.

5 CONCLUSIONS AND DISCUSSIONS

In this paper, we study the anisotropic cosmic expansion in a model-independent way. The data we use are the combination of SNe Ia Union 2.1 and 116 GRB samples. The luminosity distance is expanded with model-independent cosmography parameters: Hubble (H), deceleration (q), jerk (j) and snap (s) parameters. These cosmographic parameters obtained from the FRW metric are only based on the cosmological principle.

The magnitudes of dipole and monopole are $(1.37 \pm 0.57) \times 10^{-3}$ and $(2.6 \pm 2.1) \times 10^{-4}$. Our results show that the dipolar anisotropy is significant. The confidence level is 97.29%, more than 2σ , by doing 2×10^5 MC simulations. It's more significant than the results from SNe Ia Union 2 (Mariano & Perivolaropoulos 2012) and Union 2.1 data (Yang, Wang & Chu 2014) alone, which give out the probability 95.25% and 95.45%, respectively. Our results are also much more significant than the results from Cai et al. (2013), who used a combination of SNe Ia Union 2 and 67 GRBs from Liang et al. (2008) and Wei (2010). The dipolar direction in our study points to $(l = 309.2^{\circ} \pm 15.8^{\circ}, b = -8.6^{\circ} \pm 10.5^{\circ})$ in galactic coordinates for the full data. This direction is consistent with the results from Mariano & Perivolaropoulos (2012), Cai et al. (2013) and Yang, Wang & Chu (2014).

To study the anisotropy in different redshift ranges, we used two approaches: changing the redshift ranges upper or lower limits and dividing the full data into six bins. The results

are shown in Table 1, and these imply that the anisotropy is more significant at low redshift ranges. The magnitude is $(2.1 \pm 0.7) \times 10^{-3}$ in the redshift range $0.015 < z \leq 0.1$, while in the bin of $0.1 \leq z \leq 8.2$, the magnitude becomes to $(0.5 \pm 0.8) \times 10^{-3}$. The relative error of the latter is very large. Thus, the significant dipolar anisotropy of the full data is mainly caused by the low redshift sample. We also find that the magnitudes of anisotropy do not evolve with redshift, while the directions change randomly with redshift.

Since the monopole is not conspicuous, we focus on the dipolar anisotropy, and try to study its possible mechanisms. We consider two possible mechanisms: bulk flow motion model and simplified scalar perturbation metric model caused by dark energy distributions. We show their results in Table 2 and 4. Since both models can help to explain the dipolar effect, we compare our results to bulk flow surveys to break the degeneracy. We find the directions of the dipole from the bulk flow surveys are very close to our results, the average velocity and direction of the bulk flow surveys are 344.5 km s^{-1} and $(275.75^\circ, 8^\circ)$ around the scale $82.5 h^{-1} \text{ Mpc}$ (Hudson et al. 2004; Sarkar, Feldman & Watkins 2007; Watkins, Feldman & Hudson 2009; Feldman, Watkins & Hudson 2010; Ma, Gordon & Feldman 2011). Our results from SNe Ia and GRB data are 271 km s^{-1} and $(270.0^\circ, 10.2^\circ)$ on the scale of $100h^{-1} \text{ Mpc}$. Therefore, the anisotropic expansion at low redshift should be mainly caused by bulk flow motion. But the velocity $265 \pm 95 \text{ km s}^{-1}$ is too small comparing with the Hubble flow at high redshifts. Thus, bulk flow motion can be ignored at high redshift. Therefore, we cannot exclude the dipolar dark energy effects, especially at high redshift.

The dark energy dipolar scalar perturbation can affect the SNe and GRB luminosity distance on larger scales. But the redshift tomography results show the significance of anisotropy is insignificant at high redshift. The magnitude of dipole is $(6.3 \pm 8.5) \times 10^{-4}$ in redshift ranges $0.1 \leq z \leq 8.2$. Because the high-redshift sample is sparse, we cannot draw an exact conclusion that the dark energy distributes isotropically or not. Further study will need more high-redshift GRBs, since the SNe Ia cannot reach to higher than 2.0, GRBs are good probes to study cosmology at high redshift (Basilakos & Perivolaropoulos 2008; Wang & Dai 2011; Wang, Qi & Dai 2011).

ACKNOWLEDGEMENTS

We thank the referee for detailed and very constructive suggestions that have allowed us to improve our manuscript. We have benefited from reading the publicly available codes of

Mariano & Perivolaropoulos (2012). This work is supported by the National Basic Research Program of China (973 Program, grant 2014CB845800) and the National Natural Science Foundation of China (grants 11373022, 11103007, and 11033002). This research has made use of the NASA/IPAC Extragalactic Database (NED) which is operated by the Jet Propulsion Laboratory, California Institute of Technology, under contract with the National Aeronautics and Space Administration.

REFERENCES

- Antoniou I., Perivolaropoulos L., 2010, JCAP, 12, 12
- Axelsson M., Fantaye Y., Hansen F. K., Banday A. J., Eriksen H. K., Gorski K. M., 2013, ApJ, 773, L3
- Basilakos S., Perivolaropoulos L., 2008, MNRAS, 391, 411
- Bielewicz P., Górski K. M., Banday A. J., 2004, MNRAS, 355, 1283
- Blomqvist M., Mörtzell E., Nobili S., 2008, JCAP, 6, 27
- Bonvin C., Durrer R., Kunz M., 2006, PhRvL, 96, 191302
- Cai R.-G., Ma Y.-Z., Tang B., Tuo Z.-L., 2013, PhRvD, 87, 123522
- Cai R.-G., Tuo Z.-L., 2012, JCAP, 2, 4
- Campanelli L., Cea P., Fogli G. L., Marrone A., 2011, PhRvD, 83, 103503
- Cattoen C., Visser M., 2007, gr.qc, arXiv:gr-qc/0703122
- Colin J., Mohayaee R., Sarkar S., Shafieloo A., 2011, MNRAS, 414, 264
- Cooke R., Lynden-Bell D., 2010, MNRAS, 401, 1409
- Cooray A., Holz D. E., Caldwell R., 2010, JCAP, 11, 15
- Feindt U., et al., 2013, A&A, 560, A90
- Feldman H. A., Watkins R., Hudson M. J., 2010, MNRAS, 407, 2328
- Frommert M., Enßlin T. A., 2010, MNRAS, 403, 1739
- Gordon C., Land K., Slosar A., 2007, PhRvL, 99, 081301
- Gupta S., Saini T. D., Laskar T., 2008, MNRAS, 388, 242
- Gupta S., Saini T. D., 2010, MNRAS, 407, 651
- Hinshaw G., et al., 2013, ApJS, 208, 19
- Hudson M. J., Smith R. J., Lucey J. R., Branchini E., 2004, MNRAS, 352, 61
- Hutsemékers D., Cabanac R., Lamy H., Sluse D., 2005, A&A, 441, 915

- Hutsemékers D., Payez A., Cabanac R., Lamy H., Sluse D., Borguet B., Cudell J., 2011, *ASPC*, 449, 441
- King J. A., Webb J. K., Murphy M. T., Flambaum V. V., Carswell R. F., Bainbridge M. B., Wilczynska M. R., Koch F. E., 2012, *MNRAS*, 422, 3370
- Kogut A., et al., 1993, *ApJ*, 419, 1
- Koivisto T., Mota D. F., 2006, *PhRvD*, 73, 083502
- Koivisto T., Mota D. F., 2008, *JCAP*, 8, 21
- Koivisto T., Mota D. F., 2008, *ApJ*, 679, 1
- Koivisto T. S., Mota D. F., Quartin M., Zlosnik T. G., 2011, *PhRvD*, 83, 023509
- Kolatt T. S., Lahav O., 2001, *MNRAS*, 323, 859
- Li X., Lin H.-N., Wang S., Chang Z., 2013, *EPJC*, 73, 2653
- Liang N., Xiao W. K., Liu Y., Zhang S. N., 2008, *ApJ*, 685, 354
- Lineweaver C. H., Tenorio L., Smoot G. F., Keegstra P., Banday A. J., Lubin P., 1996, *ApJ*, 470, 38
- Ma Y.-Z., Gordon C., Feldman H. A., 2011, *PhRvD*, 83, 103002
- Mariano A., Perivolaropoulos L., 2013, *PhRvD*, 87, 043511
- Mariano A., Perivolaropoulos L., 2012, *PhRvD*, 86, 083517
- Perivolaropoulos L., 2014, *Galax*, 2, 22
- Planck Collaboration, et al., 2013, *arXiv*, arXiv:1303.5076
- Rathaus B., Kovetz E. D., Itzhaki N., 2013, *MNRAS*, 431, 3678
- Sarkar D., Feldman H. A., Watkins R., 2007, *MNRAS*, 375, 691
- Schwarz D. J., Weinhorst B., 2007, *A&A*, 474, 717
- Suzuki N., et al., 2012, *ApJ*, 746, 85
- Tegmark M., de Oliveira-Costa A., Hamilton A. J., 2003, *PhRvD*, 68, 123523
- Turnbull S. J., Hudson M. J., Feldman H. A., Hicken M., Kirshner R. P., Watkins R., 2012, *MNRAS*, 420, 447
- Visser M., 2004, *CQGra*, 21, 2603
- Wang F. Y., Dai Z. G., 2011, *A&A*, 536, A96
- Wang F. Y., Dai Z. G., Qi S., 2009a, *A&A*, 507, 53
- Wang F. Y., Dai Z. G., Qi S., 2009b, *RAA*, 9, 547
- Wang F. Y., Qi S., Dai Z. G., 2011, *MNRAS*, 415, 3423
- Watkins R., Feldman H. A., Hudson M. J., 2009, *MNRAS*, 392, 743
- Webb J. K., King J. A., Murphy M. T., Flambaum V. V., Carswell R. F., Bainbridge M. B.,

2011, PhRvL, 107, 191101

Wei H., 2010, JCAP, 8, 20

Yang X. F., Wang F. Y., Chu Z., 2014, MNRAS, 437, 1840

| GRB | redshift | $\mu \pm \sigma_\mu$ | h | m | s | ° | ' | " | GRB | redshift | $\mu \pm \sigma_\mu$ | h | m | s | ° | ' | " |
|---------|----------|----------------------|----|----|------|-----|----|----|---------|----------|----------------------|----|----|------|-----|----|----|
| 030329 | 0.17 | 39.57 ± 0.65 | 10 | 44 | 50 | 21 | 31 | 18 | 990510 | 1.62 | 45.53 ± 0.46 | 13 | 38 | 3 | -80 | 29 | 44 |
| 050826 | 0.3 | 40.97 ± 1.61 | 5 | 51 | 1.6 | -2 | 38 | 35 | 080605 | 1.64 | 45.21 ± 0.80 | 17 | 28 | 30 | 4 | 0 | 57 |
| 060512 | 0.44 | 41.95 ± 1.94 | 13 | 3 | 5.8 | 41 | 11 | 27 | 050802 | 1.71 | 44.87 ± 1.12 | 14 | 37 | 5.8 | 27 | 47 | 13 |
| 010921 | 0.45 | 42.01 ± 0.88 | 22 | 55 | 59.9 | 40 | 55 | 53 | 050315 | 1.95 | 45.22 ± 1.20 | 20 | 25 | 54.1 | -42 | 36 | 2 |
| 060729 | 0.54 | 42.49 ± 1.74 | 6 | 21 | 31.8 | -62 | 22 | 12 | 080319C | 1.95 | 45.74 ± 1.11 | 17 | 16 | 1.9 | 55 | 23 | 28 |
| 070521 | 0.55 | 42.55 ± 0.84 | 16 | 10 | 38.6 | 30 | 15 | 23 | 030226 | 1.98 | 46.21 ± 0.56 | 11 | 33 | 4.9 | 25 | 53 | 56 |
| 050223 | 0.59 | 42.73 ± 1.76 | 18 | 5 | 32.2 | -62 | 28 | 20 | 060108 | 2.03 | 46.67 ± 1.77 | 9 | 48 | 2 | 31 | 55 | 8 |
| 050525A | 0.61 | 42.82 ± 0.65 | 18 | 32 | 32.6 | 26 | 20 | 23 | 070611 | 2.04 | 46.65 ± 1.64 | 0 | 7 | 58 | -29 | 45 | 19 |
| 070612A | 0.62 | 42.85 ± 1.22 | 8 | 5 | 24.7 | 37 | 15 | 47 | 000926 | 2.07 | 46.53 ± 1.57 | 17 | 4 | 9.6 | 51 | 47 | 10 |
| 050416A | 0.65 | 42.99 ± 1.07 | 12 | 33 | 54.6 | 21 | 3 | 27 | 070810A | 2.17 | 45.90 ± 0.83 | 12 | 39 | 47.7 | 10 | 44 | 53 |
| 020405 | 0.7 | 43.18 ± 1.72 | 5 | 1 | 57 | 11 | 46 | 24 | 050922C | 2.2 | 46.24 ± 0.82 | 21 | 9 | 33 | -8 | 45 | 30 |
| 060904B | 0.7 | 43.18 ± 0.76 | 13 | 58 | 10 | -31 | 23 | 0 | 070506 | 2.31 | 47.96 ± 0.85 | 23 | 8 | 52.4 | 10 | 43 | 20 |
| 970228 | 0.7 | 43.20 ± 0.86 | 3 | 52 | 50.5 | 0 | 43 | 31 | 021004 | 2.32 | 47.20 ± 0.69 | 0 | 26 | 54.7 | 18 | 55 | 41 |
| 991208 | 0.71 | 43.22 ± 1.03 | 16 | 33 | 53.5 | 46 | 27 | 21 | 051109A | 2.35 | 47.79 ± 0.86 | 22 | 1 | 15.2 | 40 | 49 | 23 |
| 041006 | 0.71 | 43.22 ± 0.76 | 0 | 54 | 50 | 1 | 7 | 14 | 070110 | 2.35 | 47.33 ± 1.62 | 0 | 3 | 39.3 | -52 | 58 | 27 |
| 061110A | 0.76 | 43.37 ± 0.84 | 22 | 25 | 9.8 | -2 | 15 | 31 | 060908 | 2.43 | 45.99 ± 1.32 | 2 | 7 | 18.3 | 0 | 20 | 31 |
| 080430 | 0.77 | 43.40 ± 1.73 | 11 | 1 | 14.6 | 51 | 41 | 8 | 080310 | 2.43 | 46.18 ± 0.83 | 14 | 40 | 9.8 | 0 | 9 | 54 |
| 030528 | 0.78 | 43.47 ± 0.87 | 17 | 4 | 2 | -22 | 38 | 59 | 080413A | 2.43 | 46.25 ± 0.81 | 19 | 9 | 11.7 | -27 | 40 | 41 |
| 051022 | 0.8 | 43.54 ± 0.73 | 23 | 56 | 4.2 | 19 | 36 | 32 | 050406 | 2.44 | 46.32 ± 2.10 | 2 | 17 | 52.2 | -50 | 11 | 16 |
| 070508 | 0.82 | 43.61 ± 0.82 | 20 | 51 | 11.8 | -78 | 23 | 5 | 070802 | 2.45 | 47.33 ± 1.65 | 2 | 27 | 36.9 | -55 | 31 | 5 |
| 050824 | 0.83 | 43.64 ± 3.85 | 0 | 48 | 56.1 | 22 | 36 | 33 | 030115 | 2.5 | 46.79 ± 0.88 | 11 | 18 | 30 | 15 | 2 | 0 |
| 970508 | 0.84 | 43.66 ± 1.09 | 6 | 53 | 28 | 79 | 17 | 24 | 070529 | 2.5 | 47.31 ± 1.59 | 18 | 54 | 58.2 | 20 | 39 | 34 |
| 990705 | 0.84 | 43.67 ± 0.66 | 5 | 9 | 54.8 | -72 | 7 | 54 | 080721 | 2.6 | 47.28 ± 0.86 | 14 | 57 | 55.8 | -11 | 43 | 25 |
| 060814 | 0.84 | 43.67 ± 0.79 | 14 | 45 | 21.3 | 20 | 35 | 11 | 050820A | 2.61 | 46.98 ± 0.54 | 22 | 29 | 38.1 | 19 | 33 | 37 |
| 070318 | 0.84 | 43.67 ± 0.85 | 3 | 13 | 56.8 | -42 | 56 | 46 | 080210 | 2.64 | 46.96 ± 0.90 | 16 | 45 | 2.4 | 13 | 49 | 30 |
| 000210 | 0.85 | 43.70 ± 1.04 | 1 | 59 | 15.6 | -40 | 39 | 33 | 030429 | 2.66 | 46.96 ± 0.79 | 12 | 13 | 7.5 | -20 | 54 | 50 |
| 040924 | 0.86 | 43.74 ± 0.87 | 2 | 6 | 22.5 | 16 | 6 | 49 | 060604 | 2.68 | 46.66 ± 1.59 | 22 | 28 | 55 | -10 | 54 | 56 |
| 070714B | 0.92 | 43.91 ± 0.83 | 3 | 51 | 22.3 | 28 | 17 | 52 | 071031 | 2.69 | 47.22 ± 0.82 | 0 | 25 | 37.4 | -58 | 3 | 33 |
| 051016B | 0.94 | 43.96 ± 0.84 | 8 | 48 | 27.8 | 13 | 39 | 20 | 080603B | 2.69 | 47.20 ± 1.62 | 11 | 46 | 12.2 | 68 | 3 | 43 |
| 080319B | 0.94 | 43.97 ± 1.79 | 14 | 31 | 41 | 36 | 18 | 9 | 060714 | 2.71 | 47.00 ± 1.59 | 15 | 11 | 26.4 | -6 | 33 | 58 |
| 071010B | 0.95 | 43.99 ± 0.84 | 10 | 2 | 7.9 | 45 | 44 | 2 | 050603 | 2.82 | 47.35 ± 1.00 | 2 | 39 | 56.9 | -25 | 10 | 55 |
| 970828 | 0.96 | 44.03 ± 0.76 | 18 | 8 | 31.7 | 59 | 18 | 50 | 050401 | 2.9 | 47.14 ± 0.87 | 16 | 31 | 28.8 | 2 | 11 | 14 |
| 980703 | 0.97 | 44.05 ± 0.66 | 23 | 59 | 5 | 8 | 33 | 36 | 070411 | 2.95 | 47.24 ± 1.58 | 7 | 9 | 19.9 | 1 | 3 | 53 |
| 071010A | 0.98 | 44.08 ± 1.93 | 19 | 12 | 10.1 | -32 | 23 | 2 | 080607 | 3.04 | 47.55 ± 0.83 | 12 | 59 | 51.1 | 15 | 54 | 36 |
| 021211 | 1.01 | 44.16 ± 0.83 | 8 | 8 | 59.8 | 6 | 43 | 37 | 060607A | 3.08 | 46.42 ± 0.92 | 21 | 58 | 50.4 | -22 | 29 | 47 |
| 991216 | 1.02 | 44.19 ± 0.66 | 5 | 9 | 31.2 | 11 | 17 | 7 | 020124 | 3.2 | 47.16 ± 0.53 | 9 | 32 | 50.8 | -11 | 31 | 11 |
| 080411 | 1.03 | 44.21 ± 0.83 | 2 | 31 | 50.6 | -71 | 17 | 49 | 080516 | 3.2 | 47.25 ± 1.06 | 8 | 2 | 34.2 | -26 | 9 | 35 |
| 000911 | 1.06 | 44.29 ± 1.62 | 2 | 18 | 34.3 | 7 | 44 | 28 | 060526 | 3.21 | 46.23 ± 1.08 | 15 | 31 | 18.3 | 0 | 17 | 5 |
| 071003 | 1.1 | 44.38 ± 0.83 | 20 | 7 | 25.9 | 10 | 57 | 18 | 060926 | 3.21 | 47.43 ± 0.51 | 17 | 35 | 43.6 | 13 | 2 | 19 |
| 080413B | 1.1 | 44.38 ± 0.82 | 21 | 44 | 33.1 | -19 | 58 | 52 | 050908 | 3.35 | 47.33 ± 1.32 | 1 | 21 | 50.7 | -12 | 57 | 17 |
| 071122 | 1.14 | 44.47 ± 1.95 | 18 | 26 | 14.1 | 47 | 7 | 5 | 061222B | 3.36 | 47.17 ± 1.59 | 7 | 1 | 24.6 | -25 | 51 | 36 |
| 070208 | 1.17 | 44.54 ± 1.88 | 13 | 11 | 32.6 | 61 | 57 | 54 | 030323 | 3.37 | 47.52 ± 2.50 | 11 | 6 | 9.4 | -21 | 46 | 13 |
| 080707 | 1.23 | 44.67 ± 1.73 | 2 | 10 | 31.2 | 33 | 5 | 42 | 971214 | 3.42 | 47.15 ± 1.25 | 11 | 56 | 26.4 | 65 | 12 | 1 |
| 050408 | 1.24 | 44.69 ± 1.46 | 12 | 2 | 17.3 | 10 | 51 | 10 | 060707 | 3.43 | 46.99 ± 1.59 | 23 | 48 | 19 | -17 | 54 | 17 |

| GRB | redshift | $\mu \pm \sigma_\mu$ | h | m | s | ° | ' | " | GRB | redshift | $\mu \pm \sigma_\mu$ | h | m | s | ° | ' | " |
|---------|----------|----------------------|----|----|------|-----|----|----|---------|----------|----------------------|----|----|------|-----|----|----|
| 020813 | 1.25 | 44.71 ± 0.65 | 19 | 46 | 41.9 | -19 | 36 | 5 | 061110B | 3.44 | 47.61 ± 1.00 | 21 | 35 | 40.4 | 6 | 52 | 34 |
| 061007 | 1.26 | 44.73 ± 0.82 | 3 | 5 | 19.5 | -50 | 30 | 2 | 060115 | 3.53 | 47.24 ± 1.36 | 3 | 36 | 8.4 | 17 | 20 | 43 |
| 050126 | 1.29 | 44.78 ± 0.98 | 18 | 32 | 27.2 | 42 | 22 | 14 | 060605 | 3.8 | 47.24 ± 0.90 | 21 | 28 | 37.3 | -6 | 3 | 31 |
| 990506 | 1.31 | 44.82 ± 0.83 | 11 | 54 | 50.1 | -26 | 40 | 36 | 060210 | 3.91 | 47.03 ± 1.09 | 3 | 50 | 57.4 | 27 | 1 | 34 |
| 061121 | 1.31 | 44.83 ± 0.85 | 9 | 48 | 54.6 | -13 | 11 | 43 | 050730 | 3.97 | 47.43 ± 1.66 | 14 | 8 | 17.1 | -3 | 46 | 19 |
| 071117 | 1.33 | 44.86 ± 0.82 | 22 | 20 | 10.4 | -63 | 26 | 36 | 060206 | 4.05 | 47.28 ± 0.96 | 13 | 31 | 43.4 | 35 | 3 | 4 |
| 010222 | 1.48 | 44.57 ± 0.47 | 14 | 52 | 12.5 | 43 | 1 | 6 | 050505 | 4.27 | 47.36 ± 0.83 | 9 | 27 | 3.3 | 30 | 16 | 25 |
| 060418 | 1.49 | 44.47 ± 0.82 | 15 | 45 | 42.8 | -3 | 38 | 26 | 060223A | 4.41 | 48.27 ± 1.20 | 3 | 40 | 49.5 | -17 | 7 | 48 |
| 060502A | 1.51 | 44.03 ± 0.96 | 16 | 3 | 42.6 | 66 | 36 | 2 | 000131 | 4.5 | 47.75 ± 1.07 | 6 | 13 | 31.1 | -51 | 56 | 42 |
| 080330 | 1.51 | 44.10 ± 1.70 | 11 | 17 | 5 | 30 | 36 | 40 | 060510B | 4.9 | 48.24 ± 1.71 | 15 | 56 | 29.2 | 78 | 34 | 12 |
| 030328 | 1.52 | 44.60 ± 0.51 | 12 | 10 | 46 | -9 | 22 | 0 | 060522 | 5.11 | 47.85 ± 1.66 | 21 | 31 | 44.8 | 2 | 53 | 11 |
| 051111 | 1.55 | 44.92 ± 1.68 | 23 | 12 | 33.2 | 18 | 22 | 29 | 050814 | 5.3 | 47.81 ± 1.62 | 17 | 36 | 45.4 | 46 | 20 | 22 |
| 080520 | 1.55 | 45.00 ± 0.85 | 18 | 40 | 46.4 | -55 | 59 | 31 | 060927 | 5.6 | 48.25 ± 0.83 | 21 | 58 | 11.9 | 5 | 21 | 50 |
| 990123 | 1.61 | 45.11 ± 0.54 | 15 | 25 | 29 | 44 | 45 | 30 | 090423 | 8.2 | 49.30 ± 1.89 | 9 | 55 | 33.2 | 18 | 8 | 57 |

Table 5: 116 long GRBs with equatorial coordinates (Right Ascension in units of hour, minute and second and Declination in units of degree, minute and second), the equatorial coordinates are from <http://ned.ipac.caltech.edu/forms/byname.html>.